

Graphical Abstract

Fully Vectorized Linear Operator Formulation for Inverse Scattering Problems

R. G. Wueest, J. Mueller, J. Aichele, H. R. Thomsen

Highlights

Fully Vectorized Linear Operator Formulation for Inverse Scattering Problems

R. G. Wueest, J. Mueller, J. Aichele, H. R. Thomsen

- Presents a fully vectorized linear operator framework for inverse scattering in NDT.
- Relies solely on the principles of linear time-invariant (LTI) systems, avoiding the need for theoretical assumptions about wave propagation.
- Enforces periodic discrete time, enabling FFT-diagonalizable circular convolution operators which are solvable using the Tikhonov regularized inverse.
- Localizes sub-wavelength sized defects in both simulated aluminum plates and real-world CFRP plates.
- Post-calibration, only sparse sensor measurements are needed for rapid health monitoring.

Fully Vectorized Linear Operator Formulation for Inverse Scattering Problems

R. G. Wueest^{a,*1} (Researcher), J. Mueller^b (Advisor), J. Aichele^b (Advisor) and H. R. Thomsen^{b,2} (Advisor)

^aDepartment of Physics, ETH Zürich, 8092, Zürich, Switzerland

^bDepartment of Earth Sciences, ETH Zürich, 8092, Zürich, Switzerland

ARTICLE INFO

Keywords:

inverse scattering
non-destructive testing
ultrasonic NDT
defect localization
empirical impulse response
Tikhonov regularization
structural health monitoring

ABSTRACT

We present an empirical, fully vectorized linear-operator framework for inverse scattering and validate it experimentally on a bidirectional carbon-fiber-reinforced polymer (CFRP) plate. The framework uses bonded piezoelectric transducers to emit periodic pulses and a Laser Doppler Vibrometer (LDV) for a one-time calibration scan, constructing source–receiver impulse-response operators. By enforcing a discrete, periodic time behavior, wave propagation is modeled as circular convolution, diagonalizable via the discrete Fourier transform (DFT). Defect localization is formulated as a Tikhonov-regularized linear inverse problem.

After calibration, monitoring uses only sparse measurements at the transducer locations. An iron cube glued to the plate serves as a defect proxy and is localized to a sub wavelength resolution. Computation is concentrated in the one-time calibration; subsequent evaluations require minimal data and time. Long-term, transducer-only calibration could enable fully automated structural health monitoring, and the empirical-operator concept may extend to alternative detection systems or unconventional sensing interfaces (e.g., touch-like surfaces). The approach is model-free and broadly applicable where forward modeling or digital-twin upkeep is impractical.

1. Introduction

Structural Health Monitoring (SHM) of engineered components aims to localize and characterize defects. The importance of SHM depends on the cost of failure, which is especially relevant in aviation, hence many methods of performing SHM on flat structures have been explored and documented. Among these methods, Piezoelectric sensors are promising from a commercial point of view due to their low cost. However, increased challenges are noted when monitoring CFRP components [4]. Different state of the art Methods for CFRP specifically are explored in [3].

Sparse monitoring using Piezoelectric sensors (measuring at a few strategically placed sensors) would be therefore be especially desirable, but it typically demands detailed numerical forward models that are difficult to build and maintain in composites [6]. Carbon-fiber-reinforced polymer (CFRP) plates, in particular, exhibit variability from layup and manufacturing that undermines predictive digital twins [1].

This paper validates a model-free alternative based on empirical linear operators and a fundamentally periodic time embedding. We excite the structure with bonded piezoelectric transducers and use a Laser Doppler Vibrometer (LDV) to perform a dense, one-time calibration scan that constructs source–receiver impulse-response operators. Propagation is treated on a discrete cyclic time axis so that it acts as circular convolution, diagonalized by the discrete Fourier transform (DFT). By designing the excitation to be strictly periodic and ensuring no other sources act on the object, the cyclic time embedding is valid by construction; we impose time periodic behavior in the setup, and thus the frequency treatment becomes equivalent to the time domain treatment. Within a single-scattering formulation, defect localization is solved via Tikhonov-regularized inverse[5] using only sparse monitoring data at the transducer locations.

We validate the approach experimentally on an anisotropic CFRP plate, demonstrating sub-wavelength localization from sparse measurements.

* wueestg@ethz.ch (R.G. Wueest); thomsenh@ethz.ch (H.R. Thomsen)
ORCID(s):

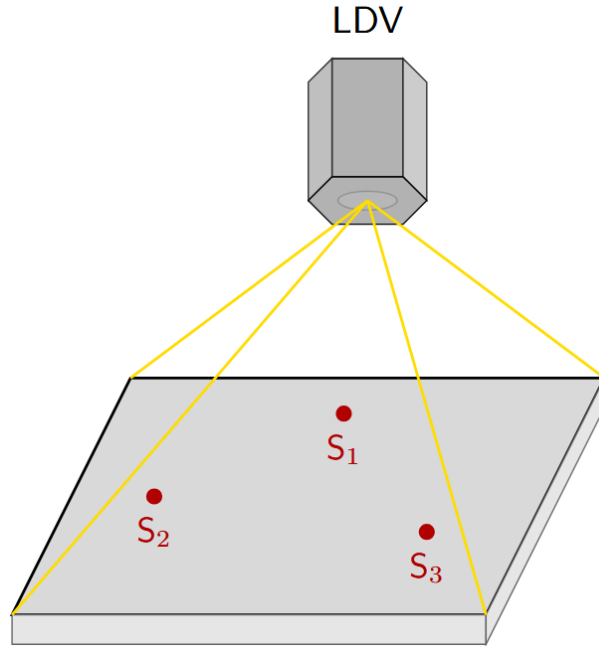


Figure 1: Experimental setup: periodic excitation with a single active transducer; an LDV scans the plate to build empirical source–receiver operators during calibration. The source pulse is taken as the self-measured excitation (including local reverberations), and periodic timing is enforced by design.

2. Methodology

The test specimen is a $25\text{ cm} \times 25\text{ cm}$ bi-directional CFRP plate, 1.3 mm thick. Five ceramic piezoelectric transducers are bonded to the plate. They are excited using an 80 kHz center-frequency Ricker wavelet pulse. An LDV scans the plate on a 104×104 grid, recording the out-of-plane velocity over time (see Figure 1). Figure 2 shows one frame of such a measurement. This scan is repeated for each of the five transducers; these acquisitions constitute the one-time calibration step.

The transducers are commercially available low-cost brass–ceramic piezoelectric discs with a nominal diameter of 12 mm. The drive is a periodic pulse train with a 2 ms repetition period, using a 80 kHz Ricker wavelet as the pulse shape to enforce timing periodicity. Data are sampled at 625 kHz and low-pass filtered to the 50 kHz prior to operator estimation. Each grid location is acquired with 10 repeats 5 separate times. I.e. we obtain 5 sets of measurements total, each having been averaged 10 times. Transducers were bonded using a hand-applied, temperature-activated adhesive; exact formulation and bond thickness were not recorded. As derived in Section 3.4, the method is independent of the source transfer function, and thus works for a wide range of unknown coupling properties.

After calibration, a 1 cm^3 iron cube is bonded to the plate to simulate a defect. During monitoring, we excite each transducer again but measure only at the transducer locations. In our setup, the LDV acquires these sparse responses at the transducer positions; in principle, the transducers themselves can act as receivers, which could enable fully automated, remote NDT/SHM. This could enable cost-effective, highly frequent SHM for important components at a press of a button. See Appendix A.5 for additional discussion of piezoelectric sensing considerations.

To characterize the plate, we estimate its dispersion. We extract an x – t slice along the axis through the active transducer from Figure 2, window the time axis to exclude edge reflections (Figure 3a), and compute a 2D FFT to obtain the k – ω spectrum. Selecting the peak-energy wavenumber $k^*(f)$ for each frequency yields the phase velocity $v_p(f) = 2\pi f / k^*(f)$ and wavelength $\lambda(f) = 2\pi / k^*(f)$ (Figure 3b). See Appendix A.3 for further comments regarding the validity of the phase velocities.

Raw data with emitter 5 at time 0.17 ms

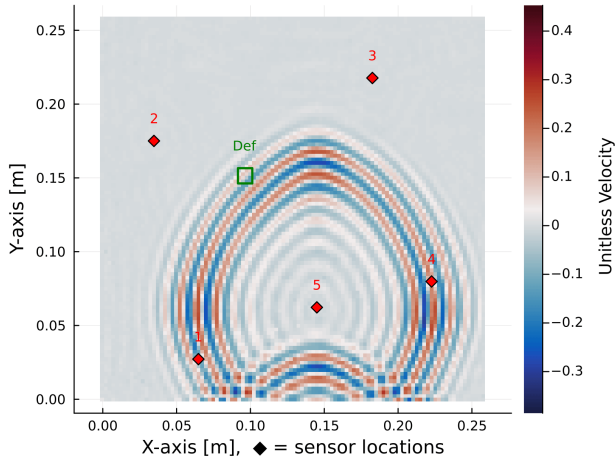
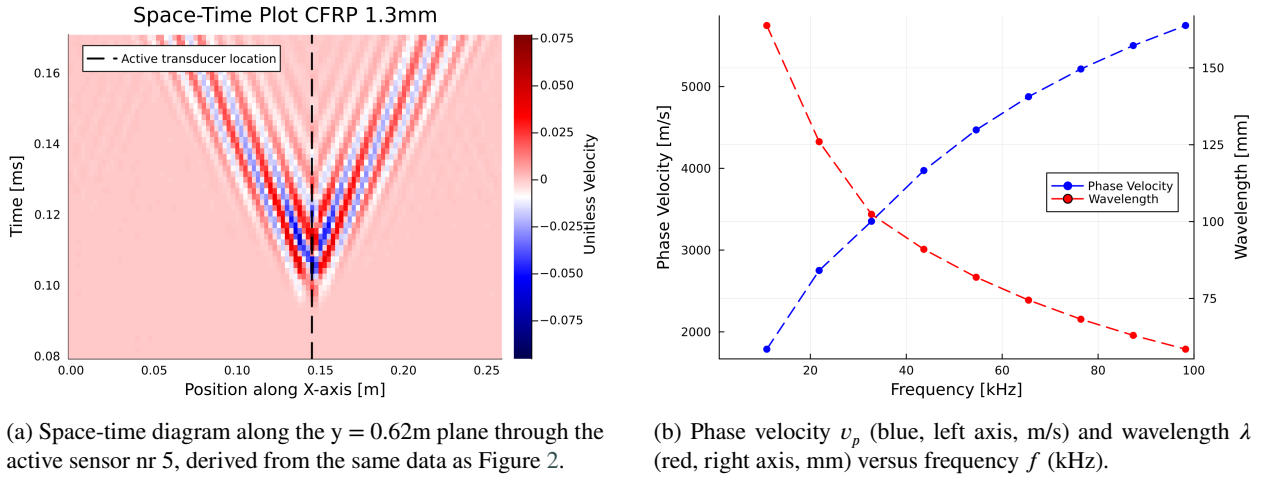


Figure 2: Snapshot of the CFRP plate at $t = 0.17$ ms, lowpass filtered to 150 kHz. Red diamonds mark the five transducers (numbered 1–5); transducer 5 is the active source. The green square indicates the location where the defect will be bonded in the monitoring phase (not yet present in this calibration scan). Note: The results in this paper employ 1–50 kHz bandpass filtering, which significantly distorts the pulse shape compared to this view; see Appendix A.1.



(a) Space-time diagram along the $y = 0.62$ m plane through the active sensor nr 5, derived from the same data as Figure 2.

(b) Phase velocity v_p (blue, left axis, m/s) and wavelength λ (red, right axis, mm) versus frequency f (kHz).

Figure 3: Empirical dispersion of the CFRP plate from the calibration scan.

3. Mathematical framework

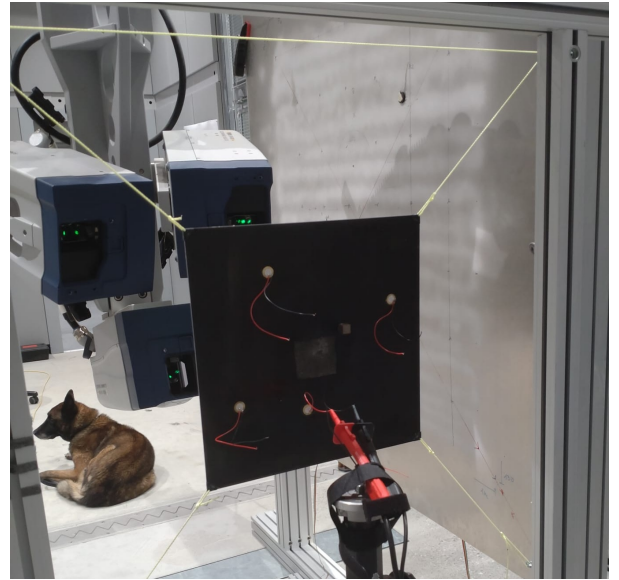
3.1. System assumptions

We assume: (i) linearity; (ii) time invariance; (iii) reciprocity; (iv) practical flatness (LDV access); and (v) the ability to control the excitation of the material relative to noise.

Assumptions (i), (ii), and (iii) are naturally satisfied for mechanical waves under standard conditions. Assumption (iv) refers to geometries where the object thickness is small relative to its lateral dimensions, typically valid for plate-like components such as aircraft fuselage panels and shell structures. Assumption (v) simply requires controlled excitation capability, which is standard in active NDT configurations using piezoelectric or electromagnetic transducers.



(a) LDV setup from the front



(b) LDV Setup from the back

Figure 4: Ich bin mir nicht sicher, ob solche bilder auch enthalten sein sollen, oder eher im Appendix mit verweis? Ein besseres bild von der hinterseite der platte wäre evtl auch noch gut, obwohl ich richtig gerne den Hund drauf behalten würde:D

3.2. Terminology and Notation

We work with discrete-time vectors and matrices throughout. The spatial domain is discretized into a set of points indexed by integers without implying any particular geometric arrangement. For instance, a 100×100 scan grid of a square plate yields 10,000 points labeled 1 through 10,000, with the specific mapping arbitrary, but fixed.

When a transducer emits a signal at location i , represented by time-domain vector \vec{s}_i , the observed signal \vec{m}_j at location j is given by the convolution with the impulse response \vec{g}_{ij} between those locations: $\vec{m}_j = \vec{g}_{ij} * \vec{s}_i$. This formulation separates spatial indices (subscripts) from the time-domain representation (vectors).

For computational implementation, these vectors correspond to discrete-time samples over a fixed acquisition window, with all operations respecting the imposed periodicity described in subsequent sections.

3.3. Periodic time and discrete representation

Repeating the excitations enforces periodicity so that the time axis can be treated on a discrete cyclic domain. Any impulse response between locations i and j is then a circular-convolution operator G_{ij} , represented by a circulant (circular Toeplitz) matrix fully determined by its first column (the sampled impulse-response vector \vec{g}_{ij}). Explicitly, for $\vec{g}_{ij} = (g_0, g_1, \dots, g_{n-1})^T$,

$$G_{ij} = \begin{pmatrix} g_0 & g_{n-1} & \cdots & g_1 \\ g_1 & g_0 & \cdots & g_2 \\ \vdots & \vdots & \ddots & \vdots \\ g_{n-1} & g_{n-2} & \cdots & g_0 \end{pmatrix} \quad (1)$$

so that $G_{ij}\vec{v} = \vec{g}_{ij} * \vec{v}$ (circular convolution). All such operators are diagonalized by the discrete Fourier transform (DFT), enabling component-wise multiplication in frequency.

3.4. Empirical impulse responses

We do not separate an “ideal” injected waveform from local reverberations at a transducer. The self-measured periodic signal \vec{s}_s is taken as the source vector. For a transducer s and measurement point i (grid or other transducer), the response is modeled as a circular convolution:

$$\vec{m}_i = G_{is}\vec{s}_s \quad (2)$$

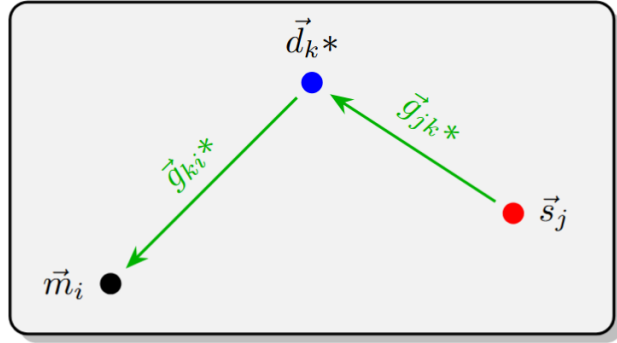


Figure 5: Visualization on how a source at location j propagates to a defect at location k , which then re-emits the wave. Afterwards, it propagates to a receiver location i . As an equation, the image visualizes $\vec{m}_i = \vec{g}_{kj} * \vec{d}_k * \vec{g}_{ik} * \vec{s}_j$.

where G_{is} is circulant (first column \vec{g}_{is}). Directional (mode) decomposition is intentionally omitted because the LDV records only the scalar out-of-plane velocity at each sampled point.

To robustly estimate \vec{g}_{is} , we use repeated measurements. Let $\{(\vec{s}_{s,p}, \vec{m}_{i|s,p})\}_{p=1}^P$ denote P repeated acquisitions. In the frequency domain (hats denote DFT components), for each frequency bin f we solve the Tikhonov-regularized least-squares problem:

$$\min_{\hat{g}_{is}(f)} \sum_{p=1}^P \left| \hat{m}_{i|s,p}(f) - \hat{s}_{s,p}(f) \hat{g}_{is}(f) \right|^2 + \alpha |\hat{g}_{is}(f)|^2 \quad (3)$$

with regularization parameter $\alpha > 0$. The closed-form solution is:

$$\hat{g}_{is}^{\text{reg}}(f) = \frac{\sum_p \overline{\hat{s}_{s,p}(f)} \hat{m}_{i|s,p}(f)}{\sum_p |\hat{s}_{s,p}(f)|^2 + \alpha} \quad (4)$$

The result is a stabilized impulse-response function that does not rely on assuming specific noise characteristics.

Notes: Although the framework is presented with LDV-acquired empirical impulse responses, the same operators G_{ij} can be generated computationally from an analytical model or a digital twin (e.g., FEM/FDTD). In that case, emitter and receiver coupling, as well as the enforced periodicity, must be accounted for separately.

3.5. Defect model

Since defects also satisfy the assumptions in Section 3.1, their effects can be modeled using circular convolutions. Within the single-scattering (Born-type) approximation, the scattering process is illustrated in Fig. 5. For clarity, we first assume a *delta-like* (instantaneous) temporal reflection kernel, so each defect is represented by a scalar amplitude d_k at its spatial location. Algebraically, this corresponds to selecting only the first canonical temporal basis vector \vec{e}_0 . This is a **defect-basis choice** made for pedagogical clarity, not a limitation of the framework. The generalization to richer local bases is presented in Section A.6 after the main operator assembly and inversion.

3.6. Operator assembly

For an emitter at j and a measurement at i , the measured signal consists of a direct propagation term and first-order (single-scattered) contributions, as illustrated in Fig. 5:

$$\vec{m}_i = \vec{g}_{ij} * \vec{s}_j + \sum_{k=1}^N \vec{g}_{ik} * \vec{d}_k * \vec{g}_{kj} * \vec{s}_j. \quad (5)$$

Which can be rewritten in matrix form:

$$\vec{m}_i = G_{ij} \vec{s}_j + \sum_{k=1}^N G_{ik} D_k G_{kj} \vec{s}_j. \quad (6)$$

Using the commutativity of circular convolution, restate the problem as

$$\Delta \vec{m}_{ij} := \vec{m}_i - G_{ij} \vec{s}_j = \sum_{k=1}^N (G_{ik} G_{kj} S_j) \vec{d}_k. \quad (7)$$

Writing the defect vectors \vec{d}_k as a single vector:

$$\vec{\mathbf{d}}_{\text{full}} := \begin{bmatrix} \vec{d}_1 \\ \vec{d}_2 \\ \vdots \\ \vec{d}_N \end{bmatrix} \quad (8)$$

The problem can be restated as a matrix problem with

$$L_{ij}^{\text{gen}} := [G_{i1} G_{1j} S_j \mid G_{i2} G_{2j} S_j \mid \dots \mid G_{iN} G_{Nj} S_j] \quad (9)$$

so that

$$\Delta \vec{m}_{ij} = L_{ij}^{\text{gen}} \vec{\mathbf{d}}_{\text{full}}. \quad (10)$$

This system is typically massively under determined, and even if not too massive for practical computing.

However, knowing that scatterers generally re-emit waves almost immediately, we can restrict the defect vectors \vec{d}_k around a small set of temporal basis functions. As mentioned in the previous section, we continue with the simplest case where $\vec{d}_k = d_k * \vec{e}_0$, i.e., a 1D basis. Since every defect at any location is parameterized by a single parameter d_k , the full defect vector can be represented as

$$\vec{\mathbf{d}} := \begin{bmatrix} d_1 \\ d_2 \\ \vdots \\ d_N \end{bmatrix} \quad (11)$$

and integrated into the problem by including the basis vectors into the problem:

$$L_{ij} := [G_{i1} G_{1j} S_j \vec{e}_0 \mid G_{i2} G_{2j} S_j \vec{e}_0 \mid \dots \mid G_{iN} G_{Nj} S_j \vec{e}_0], \quad (12)$$

where \vec{e}_0 in this equation is to be understood as a column vector. The final problem statement is then

$$\Delta \vec{m}_{ij} = L_{ij} \vec{\mathbf{d}}. \quad (13)$$

Stacking the selected (i, j) pairs yields the global residual system

$$\mathbf{m}_{\text{full}} = L_{\text{full}} \vec{\mathbf{d}}, \quad (14)$$

Here, "stacking" means vertically concatenating the pairwise residual vectors and their corresponding block-row operators, e.g.,

$$\mathbf{m}_{\text{full}} = \begin{bmatrix} \Delta \vec{m}_{12} \\ \Delta \vec{m}_{13} \\ \vdots \end{bmatrix}, \quad L_{\text{full}} = \begin{bmatrix} L_{12} \\ L_{13} \\ \vdots \end{bmatrix}$$

How the stacking is performed in practice depends on how many sensors/emitters are available and how the system is set up.

We have reduced the problem statement to the linear system in (14). The only approximations made are the discretization of space and the assumption of first-order scattering.

3.7. Regularized inversion

Let $\mathcal{L} = L_{\text{full}}$ and $\mathbf{m} = \mathbf{m}_{\text{full}}$. We estimate the defect vector by minimizing the penalized least-squares functional.

$$J(\mathbf{d}) = \|\mathcal{L}\mathbf{d} - \mathbf{m}\|_2^2 + \lambda \|\Gamma^{1/2}\mathbf{d}\|_2^2, \quad (15)$$

where $\Gamma \succeq 0$ specifies the penalty metric (a weighting / masking matrix) and $\lambda > 0$ controls the trade-off between data fit and stabilization. The normal equations yield the closed form

$$\hat{\mathbf{d}} = (\mathcal{L}^T \mathcal{L} + \lambda \Gamma)^{-1} \mathcal{L}^T \mathbf{m}. \quad (16)$$

In practice Γ is diagonal with ones everywhere except zeros at transducer locations along with a small exclusion zone around them, so those coefficients are unpenalized. This allows the inversion to self-correct for slight inconsistencies in the emitter pulse form. When plotting the defect vector as a heatmap during evaluation, these regions are omitted from the plot by setting to 0, as otherwise, these regions would dominate the results.

4. Results

Figure 6a shows the reconstructed defect vector $\tilde{\mathbf{d}}$, where each pixel represents the absolute value at a spatial grid point. After solving equation 14, the resulting vector assigns a reflection amplitude to every grid point. In this case, the vector has $101 \times 104 = 10,816$ entries, one per grid point. For visualization, each grid point is mapped back onto the 2D plane according to its original arrangement. The heatmap displays the absolute value at each location, which can be interpreted as the amplitude with which the incoming wave is reflected. No phase information is preserved, as the vector is complex-valued. The algorithm does not know the spatial correspondence of each index, and the system is not restricted to a 2D plane.

The defect in Figure 6a is clearly localized near the target location (yellow square). Small black regions appear around each transducer (red diamonds); these exclusion zones correspond to the unpenalized region in the regularization (Section 3.7) and are masked in the visualization. Behind this mask, the heatmap would show very high values, but these mostly reflect systematic errors in the experiment setup, such as differences in pulse amplitude between calibration and monitoring.

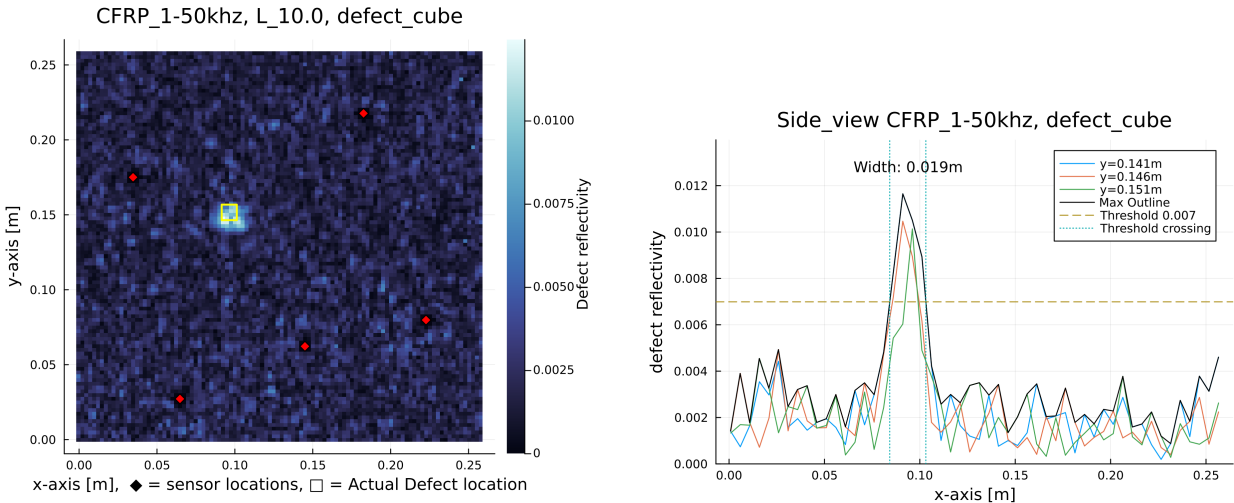
The result demonstrates successful localization of the $1 \times 1 \times 1 \text{ cm}^3$ iron cube using only sparse measurements at the five transducer locations. The particle velocity data was bandpass filtered to 1–50 kHz and processed via the Tikhonov-regularized inversion described in Section 3.7.

Figure 6b provides cross-sectional views along the x-axis. Slices exceeding 0.6 times the maximum amplitude are retained, and their envelope is drawn. This threshold identifies the localization width: the defect signature has a half-width of approximately 2 cm.

5. Discussion

The reconstructed defect has a half-width of approximately 2 cm compared to a wavelength of $\lambda_{50} \approx 8 \text{ cm}$ at 50 kHz (Figure 3b), yielding sub-wavelength localization. This is notably below the wavelength scale. The reasons for this property have prompted considerable discussion, and it remains challenging to provide a concise explanation, especially since it is difficult to demonstrate why something does *not* occur. Based on the mathematical methodology used which does not rely on explicit spatial information, there appears to be no inherent restriction enforcing a wavelength limit. In contrast, other methods often have such restrictions, typically due to the need to reconstruct measured waves in space. For example, [2] describes a method with this limitation, though it is not explicitly discussed there.

However, in the simulation study, a decrease in resolution is observed at lower frequencies, which suggests that the method is not entirely independent of wavelength-related limits. The discussion is complicated by the fact that changing the frequency bandwidth simultaneously affects three factors: the maximum frequency, the amount of information available due to the system matrix shape (see Eq. 14), and increased susceptibility to standard norm-based regularization, which can smear the result because neighboring points respond more similarly at longer wavelengths. For all intents and purposes, the method does have a resolution limitation as a function of frequency, but it is also dependent on other variables, without a hard cutoff based on frequency alone, such as with the Nyquist sampling theorem. Given the proof-of-concept nature of this paper, we refrain from exploring this topic in depth, simply noting that it is possible to isolate each variable to obtain definite answers if desired.



(a) Reconstructed magnitude of the defect vector $|\vec{d}|$ in the 1–50 kHz band. Red diamonds mark the five transducer locations; the yellow square indicates the actual location where the iron cube was bonded. The black regions around transducers are the unpenalized exclusion zones from the regularization.

(b) Cross-sectional profiles along the x-axis through the reconstructed defect (left panel). Colored envelopes show slices with amplitude exceeding 0.6 times the maximum. The localization width is estimated from the 0.6 amplitude threshold, yielding a half-width of approximately 2 cm.

Figure 6: Defect localization results in the 1–50 kHz band using sparse transducer measurements. Left: full 2D reconstruction showing sub-wavelength localization of the defect. Right: cross-sectional analysis quantifying the localization width.

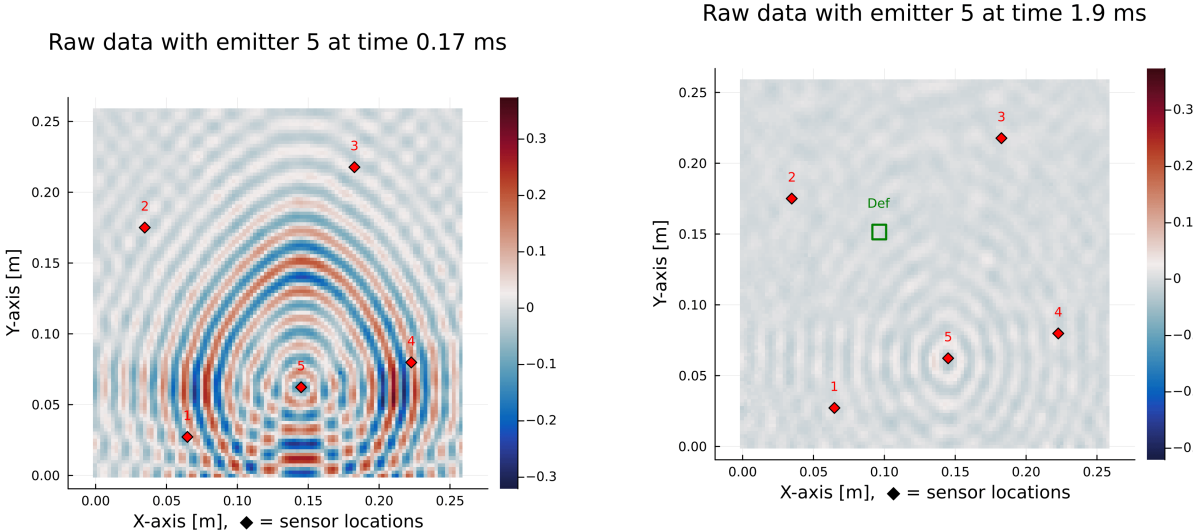
The unpenalized region around transducers (Section 3.7) was necessary to suppress phantom defects in early inversions. Pulse-shape measurements confirmed slight temporal and amplitude variations between calibration and monitoring phases. Rather than correcting these variations explicitly, the inversion absorbs them locally in the unpenalized zones.

Testing with extended frequency ranges showed that the 1–80 kHz band yields only modest quality improvements over 1–50 kHz, while extending to 1–150 kHz causes severe reconstruction degradation. Analysis of the 100–150 kHz band alone yields poor results, indicating that this frequency range carries no useful information for defect localization in the current setup. The 1–50 kHz range working similarly well to 1–80 kHz is especially interesting considering that the system matrix to be solved in equation 14 has dimensions 1000×10816 . The inversion problem is highly underdetermined by a factor of over 10. Further discussion can be found in Appendix A.4.

A key source of degradation at higher frequencies is likely misalignment between the calibration and monitoring phases. During calibration, the LDV scans a dense 104×104 grid. During monitoring, the LDV measures at transducer locations only, and realignment relies on visual cues, introducing small spatial offsets. Such misalignments couple strongly to phase information at shorter wavelengths. Notably, this alignment issue would be eliminated entirely if monitoring were performed using the transducers themselves as receivers rather than the LDV, as discussed in Section A.5.

The absolute pixel values in Figure 6a should be interpreted as relative indicators of defect location rather than quantitative scattering amplitudes. The regularization parameter λ significantly influences amplitude scaling, and the total defect effect depends on all spatial components jointly. Future quantitative work would require amplitude-density analysis and regularization-artifact correction; here, the focus is on successful localization from sparse data.

Working effectively in the 1–50 kHz band validates the empirical-operator concept, even with practical imperfections such as pulse-shape drift and measurement misalignment. The robustness in this band supports our initial hypothesis: circumventing detailed forward models in favor of empirical operators leads to numerically robust properties in the detection algorithm, allowing imperfections to be absorbed into the interpretation of the measured quantities themselves. By removing explicit spatial information entirely (the algorithm does not know about the spatial relations between each grid point), it naturally removes restrictions caused by the frequency-to-pulse-width relation, allowing us to work at low frequencies, which in turn leads to numerical robustness.



(a) CFRP plate response at $t = 0.17$ ms, bandpass filtered to 1–50 kHz. Transducer 5 is active. Compared to the unfiltered snapshot in Figure 2, the pulse is significantly broadened due to the lowpass filtering.

(b) Same setup at $t = 1.9$ ms, near the end of the 2 ms period. The pulse tail from the current repetition is still visible, and the pulse from the next repetition (nominally starting at $t = 0.12$ ms) is already present, demonstrating the wraparound inherent in the periodic time treatment.

Figure 7: Effect of 1–50 kHz bandpass filtering on the transducer pulse shape in the periodic time framework.

6. Conclusion

A. My Appendix

A.1. Low Frequency data

The results presented in the main paper employ a 1–50 kHz bandpass filter, which differs significantly from the unfiltered calibration data shown in Figure 2. Figure 7a shows the same acquisition time point, but after lowpass filtering to 50 kHz. The pulse duration expands dramatically, becoming so long that it wraps around within the periodic time window. At the end of the 2 ms period ($t \approx 1.9$ ms), the pulse from the next repetition is already visible (Figure 7b). This behavior illustrates a key strength of the framework: the algorithm does not require short, well-separated pulses. Instead, it relies on the imposed periodicity and the circulant operator structure, which naturally accommodate extended pulse durations. The periodic time treatment is therefore not merely a computational convenience but is fundamentally embedded in the mathematics of the inverse problem.

A.2. Previous results from simulations

Prior to the experiments presented here, the method was validated using commercial finite-element simulations of a 9 mm-thick rectangular aluminum plate. Defects were modeled as localized reductions in density; two representative cases are shown in Figures 8 and 9.

The simulated reconstructions reproduce the main qualitative features seen in the experiments. In simulation the results remain stable at higher frequencies and do not require spatial exclusion zones beyond the transducer positions themselves (Section 3.7). The example data sets include 10% RMS Gaussian noise.

Simulations used five transducers emitting a 50 kHz Ricker wavelet with a 10 ms repetition period. Data were low-pass filtered to 0–50 kHz to match the experimental upper bound. No additional low-frequency cutoff was applied, as it was not required in the ideal case.

Case A (Figure 8) contains a tapered circular lower-density inclusion (1.5 cm diameter) and demonstrates accurate localization in an idealized setting. Case A5B (Figure 9) contains two tapered inclusions (1.5 cm and 5 cm diameters) and illustrates the method's ability to resolve multiple and larger defects simultaneously. While the

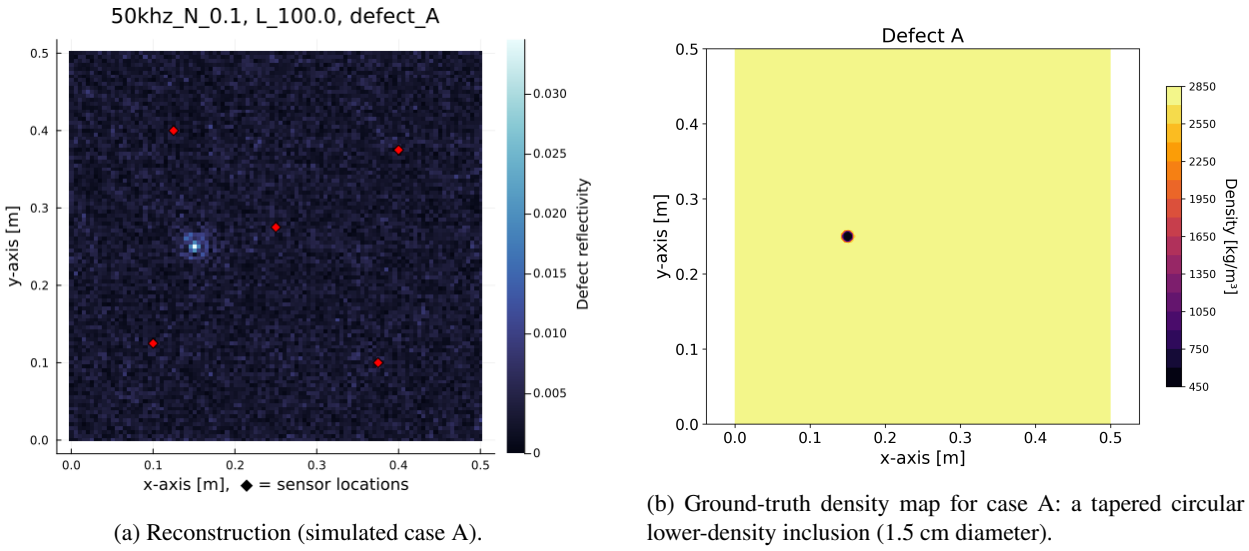


Figure 8: Simulation case A. Left: reconstruction. Right: density map. An ideal case scenario similar to the real world example.

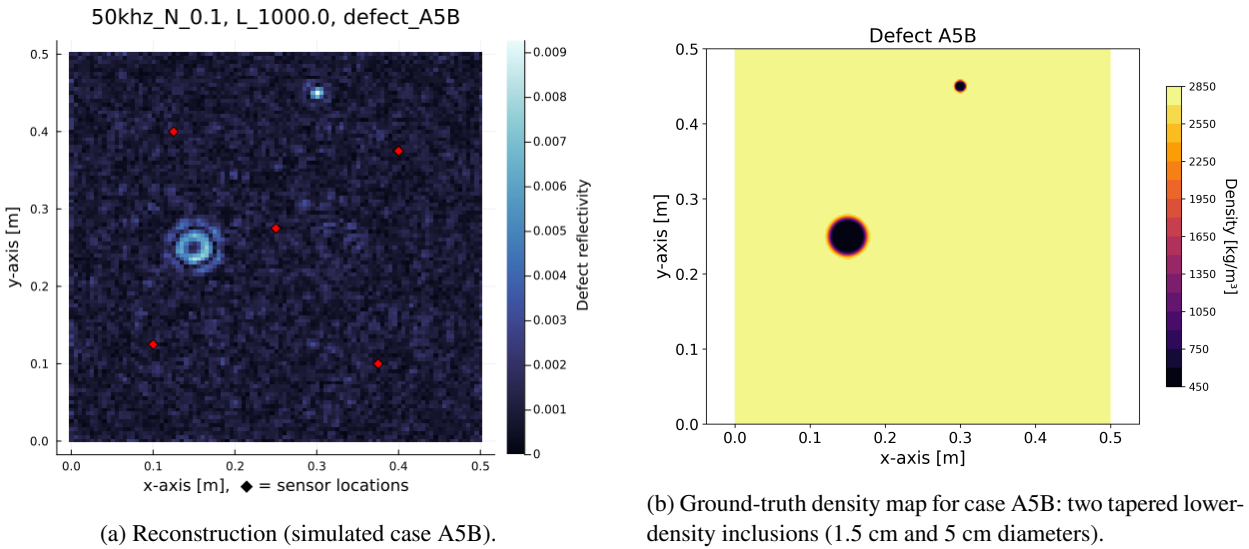


Figure 9: Simulation case A5B. Left reconstruction. Right: Density map.

simulated reconstructions are generally cleaner than the experimental results, the spatial patterns are consistent and the simulations provided useful guidance for the laboratory campaign.

Further details and additional simulation examples are documented in [7].

A.3. Discussions regarding validity of the Dispersion curve

Figures 3 suggest phase velocities that increase with frequency and reach values of order 10km/s at the upper end of the measured band. A simple Lamb-mode estimate using rough CFRP parameters places the high-frequency A0 branch near 3.8 km/s; both the empirical and theoretical numbers should be considered approximate.

The empirical estimates may be affected by measurement noise, limited angular sampling, and small alignment errors between calibration and monitoring. Conversely, the theoretical Lamb-mode calculation is only a rough ballpark because it assumes isotropic, homogeneous material properties and does not account for the plate's anisotropy or layup.

Hence discrepancies between the two are to be expected and can be substantial; neither approach alone provides a definitive “ground truth.”

For the purposes of this paper we only use phase-velocity/wavelength estimates as a rough reference to assess whether the observed localization is below the order-of-magnitude wavelength. At 50 kHz, the corresponding wavelengths are on the order of a few centimeters, and the observed localization (≈ 2 cm) remains smaller than those wavelengths. Given that this comparison is only qualitative, we do not pursue a detailed velocity validation here.

A.4. Regarding Frequencies and reconstruction

The algorithm shows limited additional benefit from including higher-frequency data, even though the measured wave spectrum extends well beyond 50 kHz, as expected from the 80 kHz central frequency of the transmitted pulses and confirmed by measurements at multiple locations on the plate. This behavior deviates from previous simulation results obtained using the same method (Appendix A.2, [7]).

As discussed in Section 5, sensor misalignment is likely to have a greater impact at higher frequencies. Additionally, the discrepancy may stem from assumptions in the problem formulation. In Section 3.5, defects are assumed to exhibit a delta-like response, implying instantaneous, frequency-independent reflection. In the simulation study, defects were modeled as changes in density, whereas the experimental defect, an adhered metal cube, more closely represents a change in stiffness, for which this assumption may be less valid.

In this context, restricting the frequency band may be advantageous: although fewer data are used, the underlying assumptions only need to hold over a narrower frequency range. However, the current experimental setup does not allow these effects to be isolated, so no definitive conclusion can be drawn.

A.5. Piezoelectric Measuring

A fully transducer-based implementation could proceed as follows: For each transducer location, two transducers are placed close together; one acts as the transmitter, the other as the sensor. During calibration, a transmitting transducer emits a periodic pulse while an LDV scans the object. The measurements from the sensing transducer are added to the LDV data and treated as an additional grid point. In the code, the sensing transducer’s measurement is assigned to the emitter location, so any coupling effects are absorbed into the object properties, potentially allowing the use of inexpensive transducers with poor coupling.

Notes: Thick, cube-shaped transducers should be avoided, as their stiffness locally alters the plate and makes measurement at or by the transducer impossible. Always use flat, plate-like ceramic transducers relative to the plate thickness.

It is important to note that the physical location of the emitting transducer and the modeled transmitter location may not coincide. This is intentional and consistent with the approach in this paper, since the LDV does not scan exactly at the transducer positions. While further decoupling the actual and modeled transducer locations is theoretically possible, it quickly becomes unstable at separations of a few centimeters. Using one emitter and multiple nearby sensing transducers, treating each sensor as an emitter in the model, may be feasible, but the practical benefit is likely limited.

A.6. Generalization to arbitrary defect bases

As mentioned in Section 3.5 and applied in Section 3.6, we assumed the defect to act as a perfect reflector of form \vec{e}_0 . In general this assumption does not hold for more complicated defects, such as delaminations in fiber-reinforced materials. In this case, using a simulation with a defect at a known location, one can compute the response nature through similar means to those described in Sections 3.6 and 3.7. Assuming we have obtained empirical defect vectors for two defect types of interest, \vec{b}_1 and \vec{b}_2 , we can implement these two vectors as a basis using a projector matrix P :

$$P := \begin{bmatrix} \vec{b}_1 & \vec{b}_2 \end{bmatrix} \quad (17)$$

Replacing \vec{e}_0 in 12, we obtain

$$L_{ij} := [G_{i1}G_{1j}S_jP \mid G_{i2}G_{2j}S_jP \mid \dots \mid G_{iN}G_{Nj}S_jP], \quad (18)$$

as well as an adjustment to the full defect vector \mathbf{d} to hold two parameters per location.

$$\mathbf{d} := \begin{bmatrix} d_{1,1} \\ d_{1,2} \\ d_{2,1} \\ \vdots \\ d_{N,2} \end{bmatrix} \quad (19)$$

where for $d_{k,b}$, k denotes the grid location, and b the basis vector at that location.

This approach is not used in this paper, as we continue using a delta-like simplifies defect. Experiments in simulation work so far has not yielded many useful bases that significantly increased performance. Especially considering the computational costs associated with increasing the defect space, as well as since we are already working in highly underdetermined systems in this paper. See [7] for further discussions into different defect bases.

References

- [1] Chen, S., Thompson, A., Dodwell, T., Hallett, S., Belnoue, J., 2025. A comparison between robust design and digital twin approaches for non-crimp fabric (ncf) forming. Composites Part A: Applied Science and Manufacturing 193, 108864. URL: <https://www.sciencedirect.com/science/article/pii/S1359835X25001587>, doi:<https://doi.org/10.1016/j.compositesa.2025.108864>.
- [2] Ebrahimkhani, A., Salamone, S., 2017. Acoustic emission source localization in thin metallic plates: A single-sensor approach based on multimodal edge reflections. Ultrasonics 78, 134–145. doi:[10.1016/j.ultras.2017.03.006](https://doi.org/10.1016/j.ultras.2017.03.006).
- [3] Han, S., Li, Q., Cui, Z., Xiao, P., Miao, Y., Chen, L., Li, Y., 2024. Non-destructive testing and structural health monitoring technologies for carbon fiber reinforced polymers: a review. Nondestructive Testing and Evaluation 39, 725–761. URL: <https://doi.org/10.1080/10589759.2024.2324149>, arXiv:<https://doi.org/10.1080/10589759.2024.2324149>.
- [4] Kosova, F., Özkan Altay, Özgür Ünver, H., 2025. Structural health monitoring in aviation: a comprehensive review and future directions for machine learning. Nondestructive Testing and Evaluation 40, 1–60. URL: <https://doi.org/10.1080/10589759.2024.2350575>, doi:[10.1080/10589759.2024.2350575](https://doi.org/10.1080/10589759.2024.2350575), arXiv:<https://doi.org/10.1080/10589759.2024.2350575>.
- [5] Tikhonov, A.N., 1963. On the solution of ill-posed problems and the method of regularization. Dokl. Akad. Nauk SSSR 151, 501–504. URL: <https://www.mathnet.ru/eng/dan/v151/i3/p501>. english translation available via MathNet.Ru.
- [6] Wan, L., Ismail, Y., Sheng, Y., Ye, J., Yang, D., 2023. A review on micromechanical modelling of progressive failure in unidirectional fibre-reinforced composites. Composites Part C: Open Access 10, 100348. URL: <https://www.sciencedirect.com/science/article/pii/S266668202300004X>, doi:<https://doi.org/10.1016/j.jcomc.2023.100348>.
- [7] Wueest, R.G., 2025. Github repository to the code, as well as further documentation. <https://github.com/Fiidch/Fully-Vectorized-Linear-Operator-Formulation-for-Inverse-Scattering-Problems>.